electric field inside a SAM through the following relationship

$$E_{in} = N(\mu_{mol}/\varepsilon d_{mol}) \quad (1)$$

where N, d_{mol} and ε are, respectively, the surface density, the height of the molecules, and the effective dielectric constant inside the monolayer (*26*, *27*). For our SP-SAM, we assumed that N is 1.8×10^{14} molecules/cm^2, ε is between 2 and 3, μ_{mol} is 6.4 D for the SP state and 13.9 D for the MC state, and d_{mol} is 2.2 nm (*13*); conversion efficiency from SP-to-MC state is ~66%. Using these values, we can estimate the difference in the electric fields (E_{in}) between the SP and MC states as 5.0 ~ 7.5 MV/cm, which is much larger than the electric fields that can be produced by applying a gate voltage using the bottom-gate structure.

To confirm this hypothesis, we performed gate voltage sweeps using the bottom-gate structure with various irradiation times. Figure 4 shows the contour plots of the resistance as a function of temperature and gate voltage for increasing times of UV light irradiation, which was performed at 5 K. The irradiation was stopped during the gate-sweep mode electrical measurement. The κ-Br device without SP-SAM was not affected by UV or visible light irradiation (fig. S9). For κ-Br devices with SP-SAM, the contour plot shifted in the positive voltage direction with elapsed UV-light irradiation time, reflecting a gradual progress of the hole carrier injection, as expected from Eq. 1. After the irradiation time of 60 s, a sudden resistance drop appeared at negative gate voltage ($V_G \approx -4$ V), showing the (field-effect assisted) photoinduced superconducting transition. When the irradiation time reached 180 s, a superconducting phase could be observed even without gate voltage. The observed voltage shift after 180 s is ~9 V, which leads to the difference in the built-in potential of 4.3 MV/cm. This value is somewhat smaller than the results obtained theoretically by Eq. 1 (5.4 ~ 8.1 MV/cm). One reason for this discrepancy is a decline of the conversion efficiency of SP-to-MC photoisomerization because of the lamination of the crystal; it is well known that the free volume around spiropyrans has an effect on the photochromic response (*28*).

Finally, a phase diagram of the κ-Br as a function of temperature and irradiation time (with applied gate voltage) was obtained by superimposing Fig. 4, A to G, as shown in Fig. 4I. We found continuous shift of the contour plots in Fig. 4, A to G, without noticeable color gradation difference in the overlapping areas. In addition, we observed a portion of a superconducting dome resembling that of the superconducting cuprates (*29*) and the κ-Br with conventional FET configuration (*20*). These results indicate that the photoinduced effect was caused not by thermal heating or interface chemical reactions but rather by the (hole) carrier doping. Furthermore, the field-induced carriers and the photoinduced carriers were working as the same type of carriers that are indistinguishable from one another in the κ-Br crystals. This means that SP-SAM EDL can expand the limit of electrostatic carrier doping beyond the density that can be accumulated only by means of a normal FET configuration.

REFERENCES AND NOTES

1. W. Schmickler, *Chem. Rev.* **96**, 3177–3200 (1996).
2. P. Simon, Y. Gogotsi, *Nat. Mater.* **7**, 845–854 (2008).
3. S. Ono, K. Miwa, S. Seki, J. Takeya, *Appl. Phys. Lett.* **94**, 063301 (2009).
4. T. Fujimoto, K. Awaga, *Phys. Chem. Chem. Phys.* **15**, 8983–9006 (2013).
5. K. Ueno *et al.*, *Nat. Mater.* **7**, 855–858 (2008).
6. J. T. Ye *et al.*, *Nat. Mater.* **9**, 125–128 (2010).
7. A. T. Bollinger *et al.*, *Nature* **472**, 458–460 (2011).
8. K. Ueno *et al.*, *Nat. Nanotechnol.* **6**, 408–412 (2011).
9. J. T. Ye *et al.*, *Science* **338**, 1193–1196 (2012).
10. V. I. Minkin, *Chem. Rev.* **104**, 2751–2776 (2004).
11. N. Tamai, H. Miyasaka, *Chem. Rev.* **100**, 1875–1890 (2000).
12. E. Orgiu, P. Samorì, *Adv. Mater.* **26**, 1827–1845 (2014).
13. H. Zhang *et al.*, *Nano Lett.* **11**, 4939–4946 (2011).
14. A. R. Jang *et al.*, *ACS Nano* **6**, 9207–9213 (2012).
15. M. Kim, N. S. Safron, C. Huang, M. S. Arnold, P. Gopalan, *Nano Lett.* **12**, 182–187 (2012).
16. A. Ikegami, M. Suda, T. Watanabe, Y. Einaga, *Angew. Chem. Int. Ed.* **49**, 372–374 (2010).
17. I. Carmeli *et al.*, *Angew. Chem. Int. Ed.* **51**, 7162–7165 (2012).
18. K. Kanoda, *J. Phys. Soc. Jpn.* **75**, 051007 (2006).
19. R. Kato *et al.*, *Chem. Lett.* **16**, 507–510 (1987).
20. H. M. Yamamoto *et al.*, *Nat. Commun.* **4**, 2379–2385 (2013).
21. Y. Kawasugi *et al.*, *Appl. Phys. Lett.* **92**, 243508 (2008).
22. Y. Kawasugi *et al.*, *Phys. Rev. Lett.* **103**, 116801 (2009).
23. H. Shinaoka, T. Misawa, K. Nakamura, M. Imada, *J. Phys. Soc. Jpn.* **81**, 034701 (2012).
24. H. Ishii, K. Sugiyama, E. Ito, K. Seki, *Adv. Mater.* **11**, 605–625 (1999).
25. D. Cahen, R. Naaman, Z. Vager, *Adv. Funct. Mater.* **15**, 1571–1578 (2005).
26. G. Ashkenasy, D. Cahen, R. Cohen, A. Shanzer, A. Vilan, *Acc. Chem. Res.* **35**, 121–128 (2002).
27. I. H. Campbell *et al.*, *Appl. Phys. Lett.* **71**, 3528–3530 (1997).
28. M. Suzuki, T. Asahi, H. Masuhara, *Phys. Chem. Chem. Phys.* **4**, 185–192 (2002).
29. N. Doiron-Leyraud *et al.*, *Nature* **447**, 565–568 (2007).

ACKNOWLEDGMENTS

Financial support for this work was provided by Grants-in-Aid for Scientific Research (S) (no. 22224006) from the Japan Society for the Promotion of Science (JSPS).

SUPPLEMENTARY MATERIALS

www.sciencemag.org/content/347/6223/743/suppl/DC1
Materials and Methods
Figs. S1 to S9

2 June 2014; accepted 14 January 2015
10.1126/science.1256783

DENTAL MATERIALS

Amorphous intergranular phases control the properties of rodent tooth enamel

Lyle M. Gordon,[1]* Michael J. Cohen,[1] Keith W. MacRenaris,[2] Jill D. Pasteris,[3] Takele Seda,[4] Derk Joester[1]†

Dental enamel, a hierarchical material composed primarily of hydroxylapatite nanowires, is susceptible to degradation by plaque biofilm–derived acids. The solubility of enamel strongly depends on the presence of Mg^{2+}, F^-, and CO_3^{2-}. However, determining the distribution of these minor ions is challenging. We show—using atom probe tomography, x-ray absorption spectroscopy, and correlative techniques—that in unpigmented rodent enamel, Mg^{2+} is predominantly present at grain boundaries as an intergranular phase of Mg-substituted amorphous calcium phosphate (Mg-ACP). In the pigmented enamel, a mixture of ferrihydrite and amorphous iron-calcium phosphate replaces the more soluble Mg-ACP, rendering it both harder and more resistant to acid attack. These results demonstrate the presence of enduring amorphous phases with a dramatic influence on the physical and chemical properties of the mature mineralized tissue.

Tooth enamel has evolved to resist the most grueling conditions of mechanical stress, fatigue, and wear (*1*). In addition, it is exposed to chemical attack in the corrosive environment of the oral cavity. Caries, or tooth decay, commonly begins with the demineralization of enamel because of production of acid by oral bacteria (*2*, *3*). Caries has an extremely high relative incidence of disease, with nearly 100% of adults worldwide having or having had caries (*4*). Although drinking water fluoridation is credited with reducing caries by an impressive 25% across all age groups, current dental expenditure in 2012 has been hovering at ~$110 billion in the United States alone (*5*). As the most prevalent chronic disease, caries thus remains an important public health problem. A substantial challenge encountered in characterizing structure and chemistry of enamel is its complex, hierarchical, and graded architecture with substantial heterogeneity in structure and composition. Closing this gap in our knowledge will aid development of quantitative models

[1]Northwestern University, Materials Science and Engineering, 2220 Campus Drive, Evanston, IL 60208, USA. [2]Northwestern University, Quantitative Bioelemental Imaging Center (QBIC), 2170 Campus Drive, Evanston, IL 60208, USA. [3]Washington University, Department of Earth and Planetary Sciences, Campus Box 1169, St. Louis, MO 63130, USA. [4]Western Washington University, Department of Physics and Astronomy, Bellingham, WA 98225, USA.
*Present address: Environmental Molecular Sciences Laboratory, Pacific Northwest National Laboratory, Post Office Box 999, Mail Stop K8-93, 3335 Innovation Boulevard, Richland, WA 99354, USA.
†Corresponding author. E-mail: d-joester@northwestern.edu

Corrected 13 February 2015; see full text.

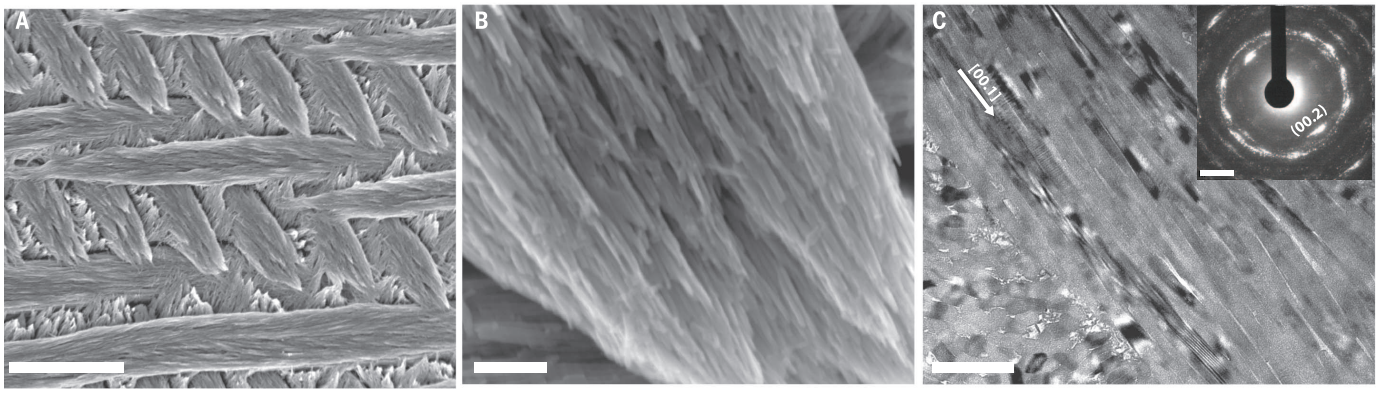

Fig. 1. Overview of mouse incisor enamel structure. (**A** and **B**) SEM images of a lactic acid–etched cross-section. (**C**) In this bright-field TEM image of a FIB-prepared thin section and (inset) selected-area diffraction pattern (SAED) of the edge of one enamel rod, alignment of nanowires parallel to the crystallographic *c* axis of the apatite lattice is apparent. Scale bars, 5 μm (A); 250 nm (B); 200 nm (C); and 2 nm^{-1} (inset).

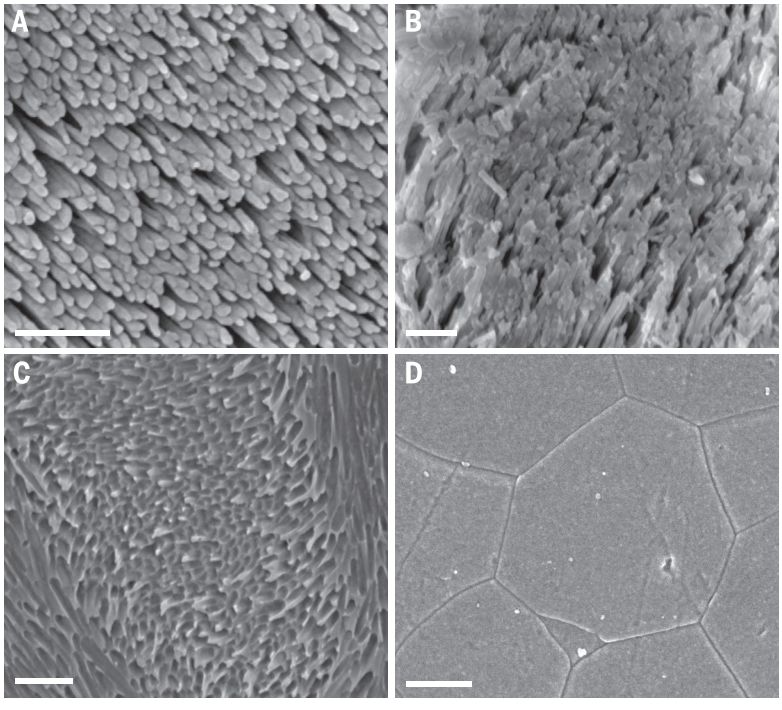

Fig. 2. SEM images of lactic acid-etched rodent enamel and sintered OHAp cross-sections. (**A**) Mouse (*Mus musculus*) incisor inner enamel. A comparison of sections before and after etching is provided in fig. S12. (**B**) Fluoride-treated mouse inner enamel. (**C**) Rat (*Rattus norvegicus*) pigmented enamel. (**D**) Sintered synthetic OHAp. Scale bars, 250 nm.

of enamel mechanical properties, connect the tissue-level etiology of caries to the underlying material structure and properties, and help innovate prophylaxis, early detection, and minimally invasive intervention.

Enamel is composed of single-crystal hydroxylapatite [OHAp, $Ca_{10}(PO_4)_6(OH)_2$] nanowires that have a rhombohedral shape with typical cross-sectional edge lengths of 25 to 50 nm (Fig. 1) (*6*, *7*). Nanowires are elongated parallel to the crystallographic [00.1] direction and have very large aspect ratios. On the order of 10^4 nanowires are bundled in rods. Rods are arranged in a dense three-dimensional (3D) weave interspersed with interrod enamel; this arrangement serves to deflect and arrest cracks (*8*). Specific features depend, among others, on location within the enamel layer of a given tooth. In the inner enamel of rodent incisors, rods are arranged in decussating layers (Fig. 1). In outer enamel, rods are packed in parallel instead and reach the enamel surface at a characteristic angle. Superimposed on the hierarchical structure, however, is a level of chemical heterogeneity that has been much more difficult to capture.

Enamel is highly mineralized at 96 weight percent (wt %) mineral, ~3 wt % water, and only ~1 wt % residual biomacromolecules (*6*). However, even small amounts of substituting ions such as magnesium (0.2 to 0.5 wt % Mg^{2+}), carbonate (2 to 4 wt % CO_3^{2-}), and fluoride (F^-) strongly affect its properties (*9*). This is commonly ascribed to substitutional defects in the OHAp lattice. For example, Mg^{2+} substitution for Ca^{2+} or CO_3^{2-} substitution for either PO_4^{3-} or OH^- results in increased solubility (*10*). Given the low solubility of fluorapatite, F^- substituting for OH^- is thought to decrease enamel susceptibility to acid attack and enhance remineralization. The concentration of these ions typically is graded over tens to hundreds of micrometers, with Mg^{2+} and CO_3^{2-} concentration increasing from the enamel surface to the dentino-enamel junction (*3*). Little is known about the distribution of ions at the length scale of rods or individual nanowires and the interfaces between them.

We used a comparative approach to understand the interplay between susceptibility to acid attack, mechanical properties, and nanoscale structure and chemistry. Rodent enamel is a generally accepted model system for human enamel (*11*). We therefore compared unpigmented "regular" rodent enamel with pigmented rodent enamel. Pigmented enamel is a reddish-brown, iron-rich type of outer enamel frequently found as an outermost layer on the incisors of rodents, shrews, and a few other species (*12*). Typically only 10 to 15 μm thick, its structural organization, but not its chemistry, is similar to that of the regular outer enamel directly underneath.

The susceptibility of enamel to dissolution in acidic environments was evaluated qualitatively by means of acid etching (*13*). Under conditions designed to approximate the intra-oral environment during carious attack, we observed that etching is highly anisotropic even at the level of individual rods (Fig. 2). In regular mouse inner enamel, etching results in a "forest" of aligned nanowires, indicating that dissolution along the boundaries between {hk.0} facets is much more rapid than at the (00.1) face. When regular enamel is topically treated with fluoride before etching, dissolution along the grain boundaries is still the prevalent mode, but the extent is reduced. Although evidence in the literature led us to expect increased resistance of pigmented enamel to acid attack (*14*), we were surprised by the dramatic effect that indicates a change in mechanism. Specifically, etching parallel to the

Corrected 13 February 2015; see full text.

grain boundaries is strongly suppressed, and slight dissolution of the nanowires on the (00.1) face leads to a characteristic honeycomb appearance in etched pigmented enamel. In contrast, etching of randomly oriented, polycrystalline OHAp with very low impurity levels is only mildly anisotropic. At comparable times of exposure to acid, only minor corrosion at the OHAp grain boundaries was observed, and there was little to no evidence of bulk dissolution or a strong dependence of etch rate on grain orientation.

We confirmed these observations through quantitative assessment of the rate at which enamel is etched. Because of their larger size, incisors from the European rabbit (*Oryctolagus cuniculus*) were used as a model for regular enamel, and from the North American beaver (*Castor canadensis*) as a model for pigmented rodent enamel. Although these organisms belong to different orders—the beaver is a rodent, and the rabbit is a lagomorph—recent evidence puts them in a monophyletic clade (Glires), and the structure of their outer enamel is similar (*15*). An additional advantage of beaver incisor is that the outer enamel is much thicker (>100 μm) than, for example, in the rat, with no noticeable structural difference in the arrangement of apatite nanowires between the outermost 10 to 15 μm of pigmented enamel and the underlying regular outer enamel (fig. S1).

A known area, typically 10 to 20 mm^2 in size, of the enamel surface was exposed to a lactic acid solution (250 mM, initial pH = 4.0, 37°C). The concentration of relevant ions in the etchant was monitored over time by using inductively coupled plasma mass spectrometry (ICP-MS) (fig. S14). The average loss of enamel mass per unit time and area was determined from time-concentration data, assuming a linear dependency, which is reasonable at short etching times. Consistent with electron microscopy and earlier qualitative observations (*14*), pigmented beaver enamel etches at a much lower rate (115 ± 15 ng mm^{-2} min^{-1}, n = 3 incisor segments) than that of regular rabbit enamel (655 ± 60 ng mm^{-2} min^{-1}, n = 3 incisor segments). At least some of this difference could in principle arise from slight structural or chemical differences in the outer enamel between the two species. However, when the regular outer enamel of the beaver was exposed with the careful mechanical removal of the pigmented layer, the etching rate was comparable with that of rabbit enamel (695 ± 60 ng mm^{-2} min^{-1}, n = 3 incisor segments). Topical treatment of the enamel so exposed with fluoride at neutral pH reduced etching rates substantially (205 ± 35 ng mm^{-2} min^{-1}, n = 3 incisor segments). However, the etch rate of fluoridated enamel is still about twice faster than that of pigmented enamel, indicating that pigmentation affords better protection against acid attack. However, remineralization in the presence of fluoride, at different pH, and over longer time periods may give different results. Taken together, the electron microscopy of etched enamel surfaces and quantitative measurement of etch rates is strong evidence that the composition of enamel is heterogeneous across the diameter of individual nanowires and that this heterogeneity affects the anisotropic etching of grain boundaries and the overall susceptibility of enamel to corrosion.

Beyond the impact on acid etching, enamel composition also affects the mechanical properties. We systematically determined enamel hardness as a function of the distance from the enamel surface using nanoindentation (fig. S2). Pigmented outer enamel of beavers and rats is harder (5 to 6 GPa, n = 3 incisors, 170 indents) than the underlying nonpigmented outer (4 to 5 GPa, n = 3 incisors, 386 indents) and inner

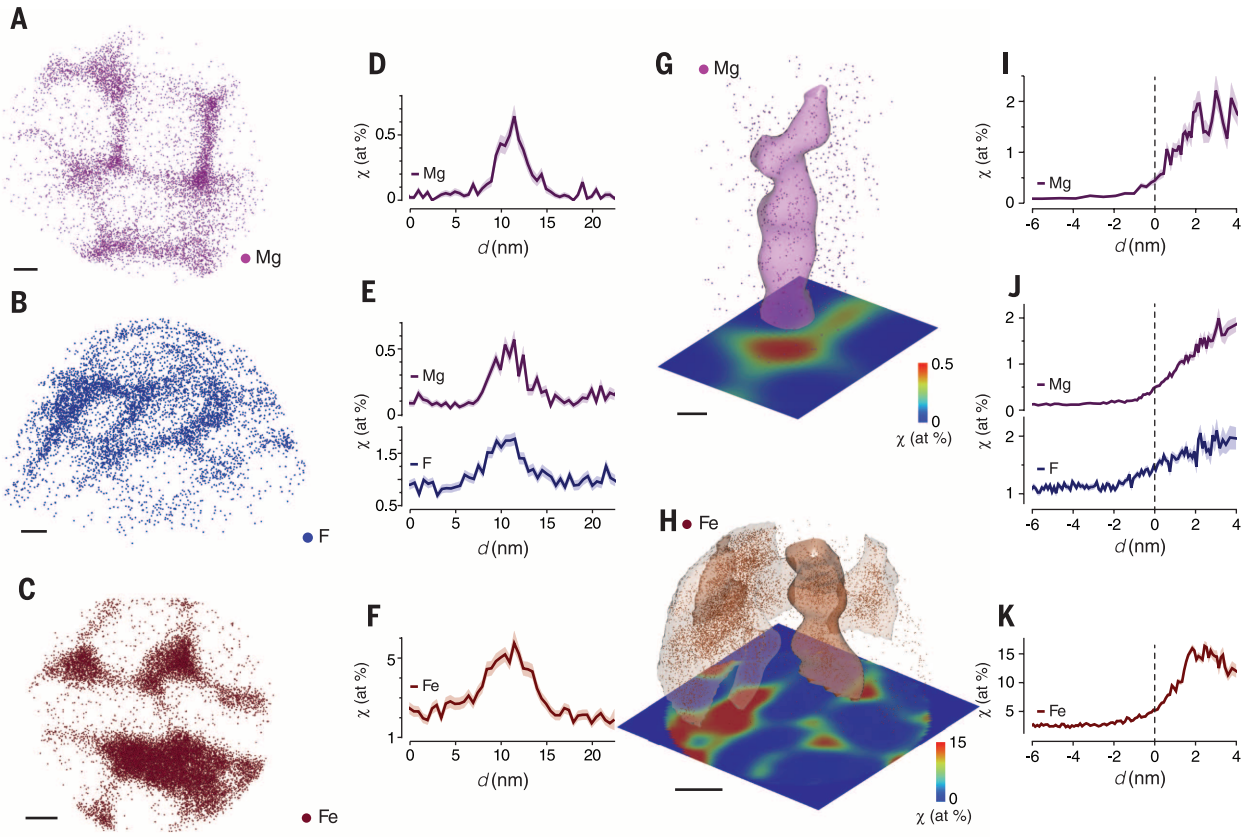

Fig. 3. APT reconstructions and compositional profiles. (**A**) Mg ($^{24}Mg^{2+}$) ion positions in mouse outer enamel. (**B**) F ($^{40}Ca^{19}F^{+}$) ion positions in fluoride-treated mouse inner enamel. (**C**) Fe ($^{56}Fe^{2+}$) ions in pigmented rat enamel. Scale bars, 10 nm. The view direction is parallel to the long axis of the nanowires. (**D** to **F**) Representative concentration profiles across grain boundaries. (**G**) Isosurface (0.5 atomic %) surrounding Mg-rich multiple grain boundary in (A). (**H**) Isosurfaces (5 atomic %) enveloping Fe-rich multiple grain boundary in (C). Scale bars in (G) and (H), 5 nm. (**I** to **K**) Representative proxigrams of multiple grain boundaries in (I) mouse outer enamel, (J) fluoride-treated outer mouse enamel, and (K) pigmented rat enamel. The distance d is relative to the isosurface. In concentration profiles and proxigrams, the solid line represents the mean and the shaded area the mean ± SD, based on counting statistics.

Corrected 13 February 2015; see full text.

enamel (4.5 GPa, n = 3 incisors, 18 indents). The hardness does not change abruptly but rather decreases gradually from the pigmented enamel surface toward the nonpigmented outer enamel. The concentration of iron is graded in the same direction (fig. S2). In rat enamel, a structural transition between the outer and inner enamel may contribute to the gradient in mechanical properties (*12*, *14*). In beaver enamel, no such transition is apparent. Furthermore, in both rat and beaver, hardness is nearly constant across the unpigmented outer enamel of the extreme mesial and distal aspect of the incisor (fig. S2). Clearly, the presence of iron has a substantial impact on enamel hardness. A likely function of the hardness gradient is to maintain a sharp edge on the continuously growing incisor (*15*).

Thus, iron not only protects enamel against acid attack but also increases mechanical hardness. Etching indicates that there are compositional differences across grain boundaries between nanowires. Atom probe tomography (APT) is a technique suited to compositional mapping at such length scales (*16*, *17*). The recent introduction of ultraviolet laser-pulsed APT has enabled the investigation of the chemical nanostructure of mineralized tissues such as the chiton tooth, bone, and dentin (*16*, *17*). During APT, single atoms or small clusters on the surface of a very sharp specimen are field-evaporated after a laser pulse. The resulting ions are projected onto an imaging detector and identified by their time of flight. The identity and position of each ion are used to create 3D reconstructions of the sample, with a spatial resolution typically better than 0.2 nm. Because of its unbiased sensitivity across the periodic table, APT is particularly powerful for samples with low-atomic-number components.

We prepared samples of inner and outer enamel from ground and polished tooth sections by means of focused ion beam (FIB) milling (*18*). APT spectra show the typical features of OHAp and a range of minor constituents, including Mg and Na in regular enamel, and Fe in pigmented enamel (fig. S3) (*17*). In 3D reconstructions, the cross sections of faceted nanowires are apparent from the distribution of minor ions (Fig. 3, A to C). At grain boundaries in regular enamel, Mg^{2+} is enriched ~20 times over the apparent solubility limit of ~0.03 atomic % in the bulk of the nanowire (table S1). This peripheral enrichment confirms earlier in vitro experiments, showing that Mg^{2+} is not readily incorporated into the apatite crystal lattice (*10*, *19*). In pigmented enamel, Fe is almost completely excluded from the interior of the nanowires (< 0.2 atomic %). No Fe was detected in regular enamel, and only trace amounts of Mg were present in pigmented enamel (table S1). Concentration profiles across the grain boundaries (Fig. 3, D to F) reveal that the concentration of minor ions is sharply elevated over a narrow region. The absolute concentration and total amount of Mg or Fe atoms at grain boundaries varies considerably, even between the boundaries on one nanowire and its neighbors. This variability may result from differences in surface energy of the particular facets but is likely also dependent on the kinetics of crystallite growth.

A convenient way to visualize the 3D distribution of impurities at multiple grain boundaries is by way of an isoconcentration surface (isosurface) (Fig. 3, G and H) that encloses a volume in which the concentration of a given ion is higher than a threshold. Proximity histograms (proxigrams) (Fig. 3, I to K) report the average mole fraction of ions as a function of distance to this surface (*20*). The physical dimensions and the exceptionally high concentration of trace ions in the associated proxigrams—~60 times the apparent solubility limit for Mg and at least 80 times the solubility limit for Fe—are strong indications that an intergranular phase that is chemically and structurally distinct from apatite is present. In regular enamel treated topically with fluoride, there is colocalization of F and Mg (Fig. 3, E and J, and fig. S13), indicating that grain boundaries and grain edges serve as short-circuit diffusion pathways. Thus, an understanding of the fundamental processes of tooth decay must account for transport along grain boundaries and the participation of the Mg-rich intergranular phase (*21*). Intergranular phases are known to strongly affect mechanical properties of ceramic materials (*22*); the increased hardness of pigmented enamel is likely a result of the structural and compositional difference of the interphase.

Although the existence of Mg-rich phases in enamel—in particular, dolomite [$CaMg(CO_3)_2$], huntite [$Mg_3Ca(CO_3)_4$], and whitlockite $Ca_9Mg(PO_4)_6(PO_3OH)$—has been proposed previously, these phases have not been observed experimentally (*19*). The strong enrichment of Mg^{2+} at interfaces and in the intergranular phase (~90% of total Mg) observed by APT allows us to use x-ray absorption spectroscopy to probe its structure. The position and intensity of transitions in Mg *K*-edge x-ray absorption near-edge structure (XANES) spectra are sensitive to the coordination number, geometry, bond length, and order at intermediate range. Many Mg-containing minerals can be identified by their spectral fingerprints (*23*). Spectra of enamel lack the pre-A, D, and E peaks that are characteristic for crystalline dolomite, huntite, and whitlockite (Fig. 4, A and B). However, the Mg-rich intergranular phase shows a striking similarity to spectra of synthetic Mg-substituted amorphous calcium phosphate (Mg-ACP), Mg/phosphate rich amorphous calcium carbonate (ACC) in the lobster cuticle, and Mg-silicate glasses (*23*, *24*). The dominant feature in spectra of these

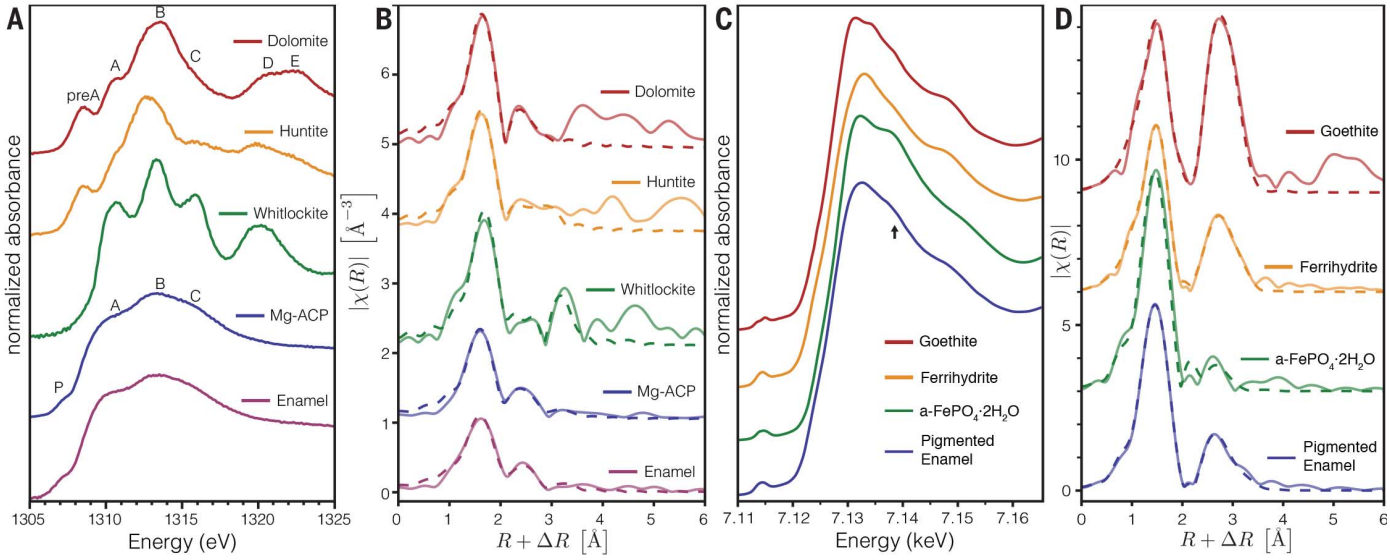

Fig. 4. X-ray absorption spectra. (**A**) Mg K-edge XANES and (**B**) k^2-weighted EXAFS spectra. (**C**) Fe K-edge XANES and (**D**) k^3-weighted EXAFS spectra. A post-edge shoulder at ~7138 eV (black arrow) appears in pigmented enamel and amorphous $FePO_4{\cdot}2H_2O$. In EXAFS spectra, fits (dashed lined) are overlaid on experimental data (solid lines).

Corrected 13 February 2015; see full text.

amorphous materials is the transition associated with the first coordination sphere (feature B), with little or no features that depend on order beyond the first shell. At the same time, the lower-edge energy is indicative of a lower coordination number and Mg-O bond distance consistent with amorphous materials.

Confirming this assessment, the Mg K-edge extended x-ray absorption fine structure (EXAFS) of enamel is nearly indistinguishable from that of synthetic Mg-ACP (Fig. 4, A and B, and fig. S4). In sharp contrast to the crystalline reference compounds, in which numerous scattering features from more distant shells are apparent, spectra of enamel and Mg-ACP are dominated by the nearest neighbor shell. Analysis of the local environment around Mg by fitting EXAFS spectra with theoretical scattering paths (table S2) reveals that the nearest-neighbor Mg-O bond lengths in enamel (2.03 Å) and Mg-ACP (2.02 Å) are notably shorter than Ca-O bonds in OHAp (2.40 Å) and ACP (2.36 Å) and also shorter than the Mg-O bonds in the crystalline reference compounds (2.08 to 2.11 Å) (*25*, *26*). However, Mg-O bonds in enamel are similar in length to Mg-O bonds observed in Mg-substituted ACC (*24*). In enamel and Mg-ACP, this shortening is accompanied by a reduction in the coordination number from 6 to ~4, which is indicative of an amorphous material and/or the presence of water in the first coordination sphere (*23*, *24*). We conclude that the environment of the majority of Mg^{2+} in enamel exhibits only short- to medium-range order, with dramatic Mg-O bond shortening, a reduction in coordination number, and the possibility of water or hydroxyl ions in the first shell, similar to the environment of Ca in ACP (*25*). Although we favor the interpretation that Mg-ACP is present as an interphase, an alternate hypothesis is that Mg^{2+} occupies disordered Ca[II] sites in apatite (*27*). In either case, the disordered environment around Mg is likely to greatly increase the solubility at the periphery of OHAp nanowires and result in anisotropic etching.

Qualitative comparison of Fe *K*-edge XANES and EXAFS spectra of pigmented beaver enamel and reference standards suggests that iron is present in a ferrihydrite-like material (Fig. 4, C and D, fig. S5, and table S2). Quantitative analysis of EXAFS along with Mössbauer (fig. S6) and Raman (fig. S7) spectroscopy confirms the presence of poorly crystalline ferrihydrite (Fh) (*28*). Because the presence of phosphate is known to inhibit growth of crystalline iron oxyhydroxides, we would expect that metastable Fh forms from any Fe(II) secreted by ameloblasts, through oxidation to Fe(III) and subsequent hydrolysis (*29*). The presence of Fh in pigmented beaver enamel is in agreement with results from nutria (*Myocastor coypus*) (*30*) but differs from the "nearly amorphous magnetite" postulated for pigmented enamel of the shrew *Blarina brevicauda*, in which pigmented enamel may have arisen through convergent evolution (*12*).

However, with both Ca^{2+} (7 to 19 atomic % Ca) and PO_4^{3-} (8 to 13 atomic % P) present in APT reconstructions of the Fe-rich intergranular phase, the material cannot be simply pure Fh. Furthermore, the stability of the intergranular phase against transformation upon heating is much greater than that of bulk Fh and leads to different products (fig. S8) (*31*). Analysis of the pre-edge region (fig. S9) reveals that the ligand field-splitting energy of pigmented enamel ($10Dq$ = 1.13 eV) is larger than that of pure ferrihydrite (0.96 eV) and a small post-edge shoulder (Fig. 4C). Both are consistent with the presence of hydrated amorphous iron phosphate (a-$FePO_4{\cdot}2H_2O$, $10Dq$ = 1.19 eV). According to linear combination analysis of EXAFS spectra, as much as 42% of the iron may be present in this form (fig. S10). Unlike the corresponding crystalline phases, amorphous phases can be very accommodating of substituents. The iron-rich interphase may thus be best described as a mixture of Fh and amorphous iron-calcium phosphate. Indeed, we observed that the interphase is strongly graded, ranging in composition from calcium-rich (Fe/Ca = 0.2) at the periphery to iron-rich (Fe/Ca = 4) in the center. Given the corrosion resistance of iron phosphates, replacing Mg-ACP with iron phosphate likely hardens pigmented enamel against acid attack (*32*).

We find that Mg^{2+} segregates at grain boundaries in regular rodent enamel, as does Fe^{3+} in pigmented enamel. We present evidence for the presence of Mg-ACP as an intergranular phase in regular enamel and of a mixture of Fh and amorphous iron-calcium phosphate in pigmented enamel. Last, we link interphase structure and composition to the resistance of pigmented enamel against acid attack and its improved hardness. In addition to the recent recognition of amorphous phases in biomineralization as transient precursors (*33*, *34*), these results demonstrate enduring amorphous phases with a dramatic influence on the physical and chemical properties of the mineralized tissue.

REFERENCES AND NOTES

1. J. L. Cuy, A. B. Mann, K. J. Livi, M. F. Teaford, T. P. Weihs, *Arch. Oral Biol.* **47**, 281–291 (2002).
2. M. A. Taubman, D. A. Nash, *Nat. Rev. Immunol.* **6**, 555–563 (2006).
3. C. Robinson *et al.*, *Crit. Rev. Oral Biol. Med.* **11**, 481–495 (2000).
4. World Health Organization, "Oral health," fact sheet (World Health Organization Media Centre, Geneva, Switzerland, 2012).
5. American Dental Association, "U.S. Dental Spending Remains Flat Through 2012," research brief (American Dental Association Health Policy Institute, 2014).
6. A. Nanci, *Ten Cate's Oral Histology: Development, Structure, and Function* (C. V. Mosby, Maryland Heights, MO, ed. 8, 2012).
7. C. B. Møinichen, S. P. Lyngstadaas, S. Risnes, *J. Anat.* **189**, 325–333 (1996).
8. S. Bechtle, S. Habelitz, A. Klocke, T. Fett, G. A. Schneider, *Biomaterials* **31**, 375–384 (2010).
9. J. D. Featherstone, S. Doméjean, *Adv. Dent. Res.* **24**, 28–31 (2012).
10. R. Z. Legfros, T. Sakae, C. Bautista, M. Retino, J. P. LeGeros, *Adv. Dent. Res.* **10**, 225–231 (1996).
11. W. H. Bowen, *Odontology* **101**, 9–14 (2013).
12. M. Dumont, T. Tütken, A. Kostka, M. J. Duarte, S. Borodin, *J. Struct. Biol.* **186**, 38–48 (2014).
13. L. M. Silverstone, C. A. Saxton, I. L. Dogon, O. Fejerskov, *Caries Res.* **9**, 373–387 (1975).
14. P. Vogel, *Rev. Suisse Zool.* **91**, 699–708 (1984).
15. T. Martin, *Zoosystemat. Evol.* **75**, 257–273 (1999).
16. L. M. Gordon, D. Joester, *Nature* **469**, 194–197 (2011).
17. L. M. Gordon, L. Tran, D. Joester, *ACS Nano* **6**, 10667–10675 (2012).
18. K. Thompson *et al.*, *Ultramicroscopy* **107**, 131–139 (2007).
19. R. A. Terpstra, F. C. Driessens, *Calcif. Tissue Int.* **39**, 348–354 (1986).
20. O. C. Hellman, J. A. Vandenbroucke, J. Rüsing, D. Isheim, D. N. Seidman, *Microsc. Microanal.* **6**, 437–444 (2000).
21. G. S. Ingram, *J. Dent. Res.* **69**, 581–586, discussion 634–636 (1990).
22. D. R. Clarke, *J. Am. Ceram. Soc.* **70**, 15–22 (1987).
23. L. Dien, P. Mingsheng, T. Murata, *Can. Mineral.* **37**, 199–206 (1999).
24. Y. Politi *et al.*, *Chem. Mater.* **22**, 161–166 (2009).
25. C. Holt *et al.*, *J. Cryst. Growth* **92**, 239–252 (1988).
26. J. M. Hughes, M. Cameron, K. D. Crowley, *Am. Mineral.* **74**, 870–876 (1989).
27. D. Laurencin *et al.*, *Biomaterials* **32**, 1826–1837 (2011).
28. J. Zhao, F. E. Huggins, Z. Feng, G. P. Huffman, *Clays Clay Miner.* **42**, 737–746 (1994).
29. J. Rose, A.-M. Flank, A. Masion, J.-Y. Bottero, P. Elmerich, *Langmuir* **13**, 1827–1834 (1997).
30. M. B. Madsen, S. Mørup, C. J. Koch, G. Lindemann, *Hyperfine Interact.* **29**, 1431–1434 (1986).
31. F. M. Michel *et al.*, *Proc. Natl. Acad. Sci. U.S.A.* **107**, 2787–2792 (2010).
32. G. Górecki, *Corrosion* **48**, 613–616 (1992).
33. L. Addadi, S. Raz, S. Weiner, *Adv. Mater.* **15**, 959–970 (2003).
34. L. Addadi, N. Vidavsky, S. Weiner, *Z. Kristallogr.* **227**, 711–717 (2012).

ACKNOWLEDGMENTS

The National Science Foundation (NSF DMR-0805313, DMR-1106208, and DMR-1341391), the Northwestern University Materials Research Center [NSF– Materials Research and Engineering Center (MRSEC) DMR-1121262], the International Institute for Nanotechnology, the Institute for Sustainability and Energy at Northwestern (ISEN), and the Petroleum Research Fund of the ACS in part supported this work. The Canadian National Sciences and Engineering Research Council in part supported L.M.G. The NIH predoctoral Biotechnology Training Grant T32GM008449 in part supported M.J.C. Portions of this work were performed at the DuPont-Northwestern-Dow Collaborative Access Team (DND-CAT) and the Canadian Light Source (CLS). DND-CAT is located at Sector 5 of the Advanced Photon Source (APS), an Office of Science User Facility operated for the U.S. Department of Energy (DOE) Office of Science by Argonne National Laboratory supported by the U.S. DOE under contract DE-AC02-06CH11357. E. I. DuPont de Nemours & Co., The Dow Chemical Company, and Northwestern University support DND-CAT. The Natural Sciences and Engineering Research Council of Canada, the National Research Council of Canada, the Canadian Institutes of Health Research, the Province of Saskatchewan, Western Economic Diversification Canada, and the University of Saskatchewan support CLS. This work made use of the Northwestern University Center for Atom Probe Tomography (NUCAPT) supported by NSF-MRI (DMR-0420532) and ONR-DURIP (N00014-0400798, N00014-0610539, N00014-0910781); the Optical Microscopy and Metallography Facility; the J. B. Cohen X-Ray Diffraction Facility supported by the NSF-MRSEC (DMR-1121262); the Northwestern University Quantitative Bioelemental Imaging Center supported by NASA Ames Research Center NNA06CB93G; the Northwestern University Atomic and Nanoscale Characterization and Experimental Center (NUANCE), Electron Probe Instrumentation Center (EPIC), and the Northwestern Nanoscale Integrated Fabrication, Testing, and Instrumentation Facility (NIFTI) supported by NSF-NSEC (EEC-0118025/003), NSF-MRSEC (DMR-1121262), the Keck Foundation, the State of Illinois, and Northwestern University. We thank Q. Ma and T. Regier for assistance with x-ray absorption spectroscopy; B. Myers for assistance with TEM sample preparation; C. Phatak for performing correlative TEM of APT samples; C. Whyne and M. Akens for supplying rat incisors; and C. Newcomb, S. Sur, and A. Deymier-Black for supplying mouse incisors. The supplementary materials contain additional data. L.M.G., J.D.P., and D.J. designed experiments, analyzed the data, and prepared the manuscript. L.M.G., M.J.C., K.W.M., J.D.P., and T.S. performed experiments.

SUPPLEMENTARY MATERIALS

www.sciencemag.org/content/347/6223/746/suppl/DC1
Materials and Methods
Figs. S1 to S14
Tables S1 to S3
References (*35*–*56*)

18 July 2014; accepted 19 December 2014
10.1126/science.1258950

Corrected 13 February 2015; see full text.

Science

Amorphous intergranular phases control the properties of rodent tooth enamel

Lyle M. Gordon, Michael J. Cohen, Keith W. MacRenaris, Jill D. Pasteris, Takele Seda and Derk Joester

Science **347** (6223), 746-750.
DOI: 10.1126/science.1258950

Key trace minerals greatly strengthen teeth

The outer layers of teeth are made up of nanowires of enamel that are prone to decay. Gordon *et al.* analyzed the composition of tooth enamel from a variety of rodents at the nanometer scale (see the Perspective by Politi). In regular and pigmented enamel, which contain different trace elements at varying boundary regions, two intergranular phases—magnesium amorphous calcium phosphate or a mixed-phase iron oxide—control the rates of enamel demineralization. This suggests that there may be alternative options to fluoridation for strengthening teeth against decay.

Science, this issue p. 746; see also p. 712

Science (print ISSN 0036-8075; online ISSN 1095-9203) is published by the American Association for the Advancement of Science, 1200 New York Avenue NW, Washington, DC 20005. The title *Science* is a registered trademark of AAAS.